Electronic Supplementary Material (ESI) for Physical Chemistry Chemical Physics.

Supplementary Information for

Direct translocation of nanoparticle across model cell membrane by nanoparticle-induced local enhancement of membrane potential

Hideya Nakamura*, Kyohei Sezawa, Masataka Hata, Shuji Ohsaki, Satoru Watano

Department of Chemical Engineering, Osaka Prefecture University,

1-1 Gakuen-cho, Naka-ku, Sakai, Osaka 599-8531, Japan

*Address correspondence to hnakamura@chemeng.osakafu-u.ac.jp (H. Nakamura)

Contents

A. Supplementary Text

B. Supplementary Figures, Tables, and Movie

C. Supplementary References

A. Supplementary Text

A.1. Molecular composition of simulation system

Tables S2 shows the molecular compositions of the simulation system used in this study. Concentrations of NaCl in both outer and inner solvent compartments were 154 mM, which is equivalent to the concentration of isotonic saline solution. Concentrations of NaCl in the outer and inner solvent compartments were identical. To compensate for the negative charge of DPPG and the positive charge of the NP, sodium and chloride ions were added to the compartments so that electroneutrality was maintained in each solvent compartment. These settings provided a zero charge imbalance and no osmotic pressure across the lipid bilayers. Amounts of DPPG in the lipid bilayer were 16 mol%, mimicking the lipid composition of human red blood cell membranes[2].

A.2. Verification of numerical calculation of electric potential

In order to verify the numerical calculation of the electric potential $\psi(\boldsymbol{x})$, the numerical calculation result was compared to the analytic solution[3]. The one-dimensional profiles of the electric potential across the lipid bilayer were compared, as shown in Fig. S2. The numerical calculation result showed good agreement with the analytic solution[3], confirming adequacy of the numerical calculation of the electric potential.

A.3. Calculation of local membrane potential at the contact interface between NP and membrane surface

To calculate the local transmembrane potential at the contact interface between the NP and the membrane surface, the following procedure was used. First, the spatial distribution of electric charge density $\rho(\boldsymbol{x})$ was calculated. The whole simulation domain was discretized into 1,155,200 rectangular cells. In each cell, the temporally- and spatially-averaged electric charge density $\rho(x)$ was calculated from trajectory data of the CG–MD simulation. Secondly, spatial distribution of the electric potential $\psi(\boldsymbol{x})$ in the whole simulation domain was calculated. By using the electric charge density $\rho(\boldsymbol{x})$ as input data, the Poisson–Boltzmann equation, $\nabla^2\psi(\boldsymbol{x}) = -\rho(\boldsymbol{x})/\varepsilon_0$ (where ε_0 is the permittivity of vacuum), was numerically solved by means of the finite difference method. The space-derivative terms were discretized using a central differencing scheme. As a computational scheme to solve the simultaneous linear equations, the SOR method was employed. Fig. S3A shows an example of the calculation result of $\psi(\boldsymbol{x})$. Finally, the local membrane potential at the contact interface between the NP and the surface of the cell membrane was calculated from $\psi(\boldsymbol{x})$. The small rectangular box with $\Delta x = \Delta y = 1.75$ nm (as shown in Fig. S3A), containing the center of mass of the NP, was set along the membrane normal (the z-axis). The rectangular box was used as the calculation domain. Fig. S3B shows the profile of the electric potential $\psi(\boldsymbol{x})$ within the calculation domain along the membrane normal. Location of the contact interface was then detected using the number-density profile of the lipid head groups and thiol terminal group of the NP. Fig. S3B also depicted the total number-density of phosphate groups of lipids (Qa depicted in Fig. S3C) and terminal groups of the NP (Qd depicted in Fig. S3C). The contact interface was defined as the z-displacement at the peak of the total number-density profile for Qa and Qd. The inner surface of the cell membrane was also defined as the z-displacement at the peak of the number density profile of lipid head groups (Q0 and P4 depicted in Fig. S3C). Finally, the local membrane potential at the contact interface was obtained as the potential difference between the contact interface and inner membrane surface, as detected by the above procedure.

A.4. Membrane potential arising from imbalance of the membrane surface charge ($\Delta\psi_{\mathrm{sci}}$)

Figs. S5A and S5B show spatial distributions of the electric potential of a cross-section of the membrane (upper lipid bilayer) without a NP. When the external electric field was applied along the negative direction of the z-axis, the electric potential at the outer surface was significantly higher than that at the inner surface (Fig. S5B), while there was no potential difference without the external electric field (Fig. S5A). Fig. S5C shows the number density of the cation (Na+) along the membrane normal. By applying the external electric field with a bias along the surface-normal axis directed towards the cell membrane (negative direction of the z-axis), more cations accumulated on the outer surface of membrane than the inner surface, inducing a higher electric potential at the outer surface with respect to the inner surface. This additional membrane potential derived from the imbalance of the membrane surface charge is referred to here as $\Delta\psi_{\mathrm{sci}}$.

A.5. Determination of critical overall membrane potential for membrane breakdown ($\Delta\psi_{\mathrm{overall,\,C}}$)

The critical overall membrane potential for membrane breakdown ($\Delta\psi_{\mathrm{overall,\,C}}$), where defect or poration in the membrane were generated without the NP, were determined from the relationship between $\Delta\psi_{\mathrm{appl}}$ and $\Delta\psi_{\mathrm{overall}}$. Fig. S6 shows the overall membrane potential $\Delta\psi_{\mathrm{overall}}$ as a function of the applied membrane potential $\Delta\psi_{\mathrm{appl}}$. Due to superimposing $\Delta\psi_{\mathrm{sci}}$ on the $\Delta\psi_{\mathrm{appl}}$, i.e., $\Delta\psi_{\mathrm{overall}} = \Delta\psi_{\mathrm{appl}} + \Delta\psi_{\mathrm{sci}}$, the $\Delta\psi_{\mathrm{overall}}$ was higher than the $\Delta\psi_{\mathrm{appl}}$. The $\Delta\psi_{\mathrm{overall,\,C}}$ was determined by extrapolating the linear relationship between the $\Delta\psi_{\mathrm{appl}}$ and $\Delta\psi_{\mathrm{overall}}$ (Fig. S6), because the $\Delta\psi_{\mathrm{overall,\,C}}$ (i.e., the $\Delta\psi_{\mathrm{overall}}$ at the $\Delta\psi_{\mathrm{appl,\,c}}$) cannot be accurately calculated due to spontaneous generation of a membrane defect and poration. Consequently, the $\Delta\psi_{\mathrm{overall,\,C}}$ was here determined as 337 mV.

A.6. Membrane-crossing of NPs with amino-OT:OT = 7:3 and 10:0

Fig. S7A shows temporal change in number of the hydrophilic lipid heads and hydrophobic lipid tails in the vicinity of the NP with amino-OT:OT = 7:3 and 10:0 during the membrane-crossing of the NP. Fig. S7B shows snapshots of the lipid molecules at the contact interface with the NPs as each NP passed across the center of the bilayer. At the vicinity of the NP with amino-OT:OT = 10:0, the number of hydrophilic lipid heads was much higher than the hydrophobic tails, while at the NP with amino-OT:OT = 7:3 the number of hydrophilic lipid heads was comparable to that of hydrophobic tails, i.e., the hydrophilic transmembrane pore was formed during the membrane-crossing of the NP with amino-OT:OT = 10:0, while the amphiphilic transmembrane pore was formed during the membrane-crossing of the NP with amino-OT:OT = 7:3. From a free energy point of view, the transformation of the planar lipid bilayer to the amphiphilic pore is energetically more favorable than the transformation to the hydrophilic pore, because the structural change in the lipid head is less. Therefore, the NP with amino-OT:OT = 7:3 was directly translocated across the cell membrane at $\Delta\psi_{\mathrm{appl}} = 161$ mV, where the local membrane potential at the contact interface was almost equivalent to the critical potential for membrane breakdown, while the NP with amino-OT:OT = 10:0 did not translocate across the cell membrane, even at $\Delta\psi_{\mathrm{appl}} = 161$ mV.

B. Supplementary Figures, Tables, and Movie

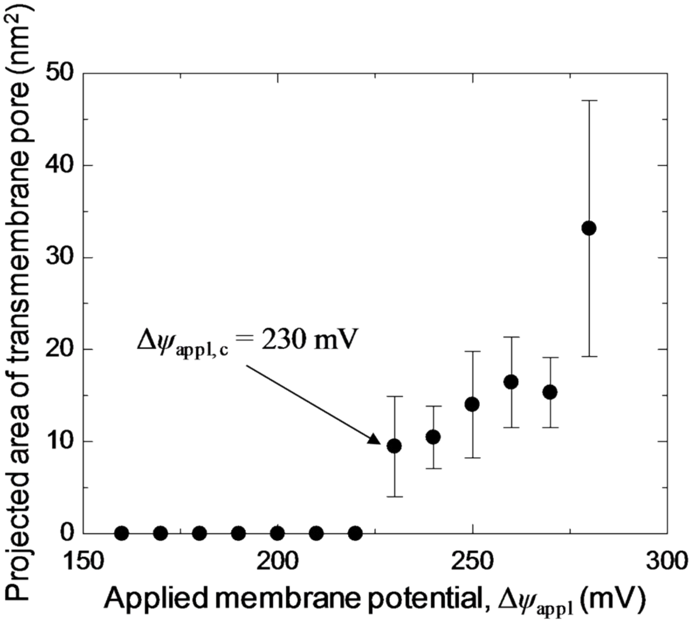

Fig. S1. Projected area of transmembrane pore as a function of applied membrane potential. To determine the critical applied potential for the membrane breakdown ($\Delta\psi_{appl,\,c}$), MD simulations without the NP were performed under several applied membrane potentials ($\Delta\psi_{appl}$). From this result, $\Delta\psi_{appl,\,c}$ was determined to be 230 mV. The $\Delta\psi_{appl,\,c}$ obtained in this study is in agreement with experimental results[1].

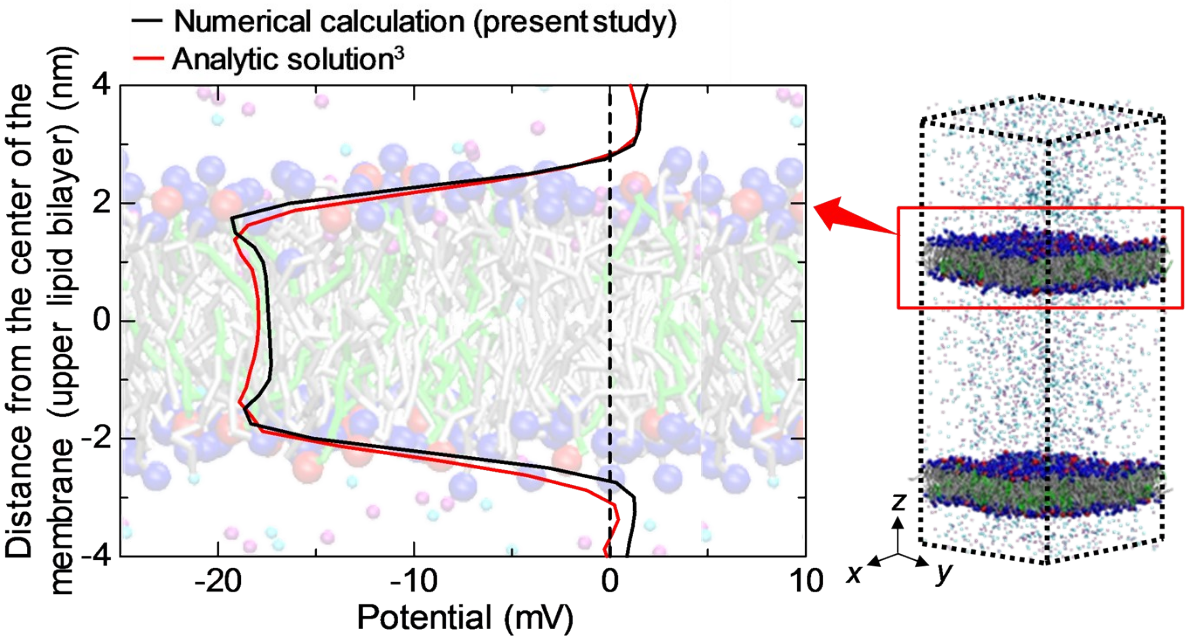

Fig. S2. One-dimensional profiles of electric potential across upper lipid bilayer. No external electric field was applied, and there was no NP.

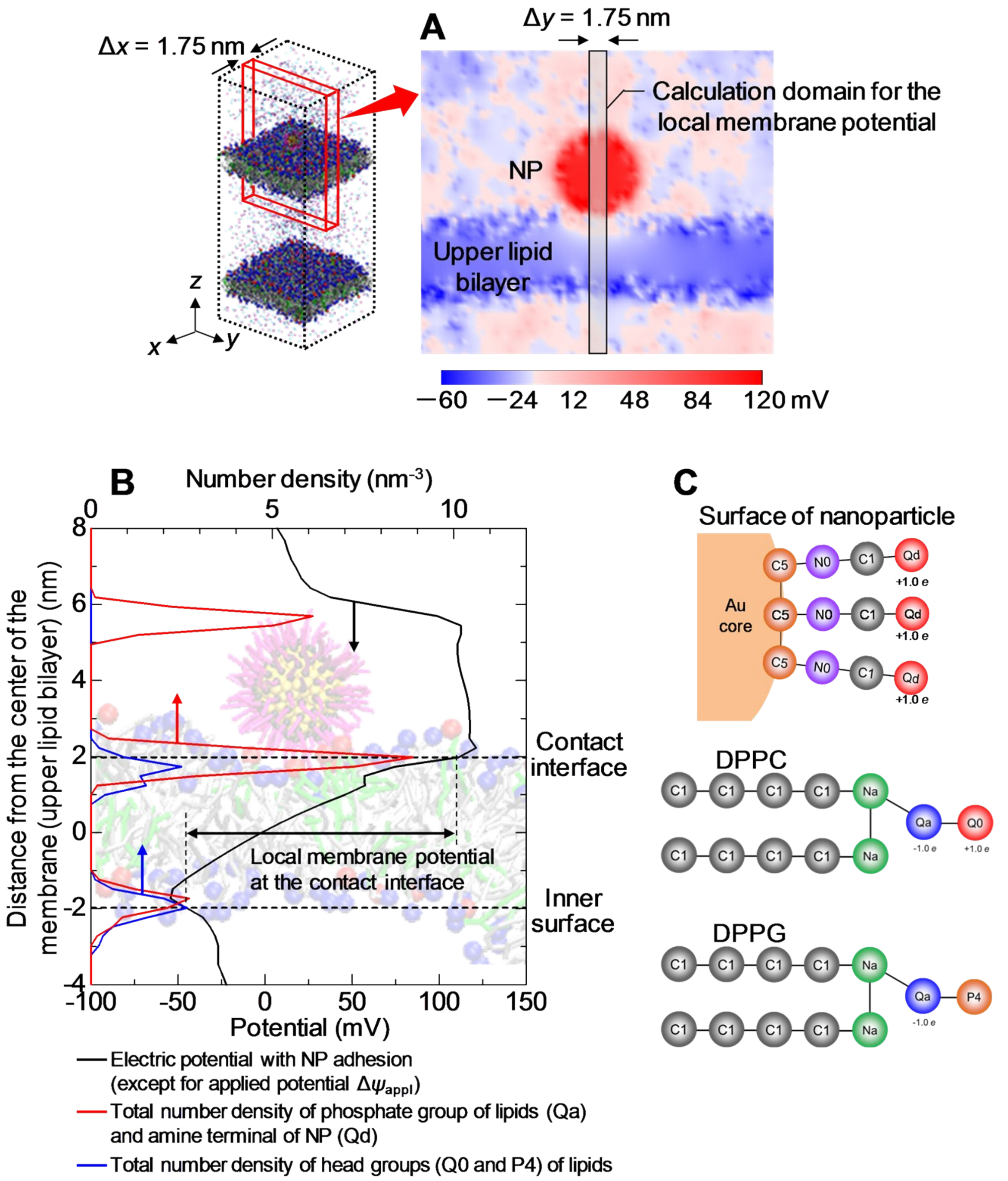

Fig. S3. Calculation of local membrane potential at the contact interface between NP and membrane surface. (A) Spatial distribution of the electric potential $\psi(\boldsymbol{x})$ in cross-sectional space. (B) Electric potential profile and number density profiles of coarse-grained sites in the calculation domain for the local membrane potential. Electric potential generated by the externally applied electric field ($\Delta\psi_{\mathrm{appl}}$) was not included. (C) Coarse-grained structure and the type of coarse-grained sites composing each molecule.

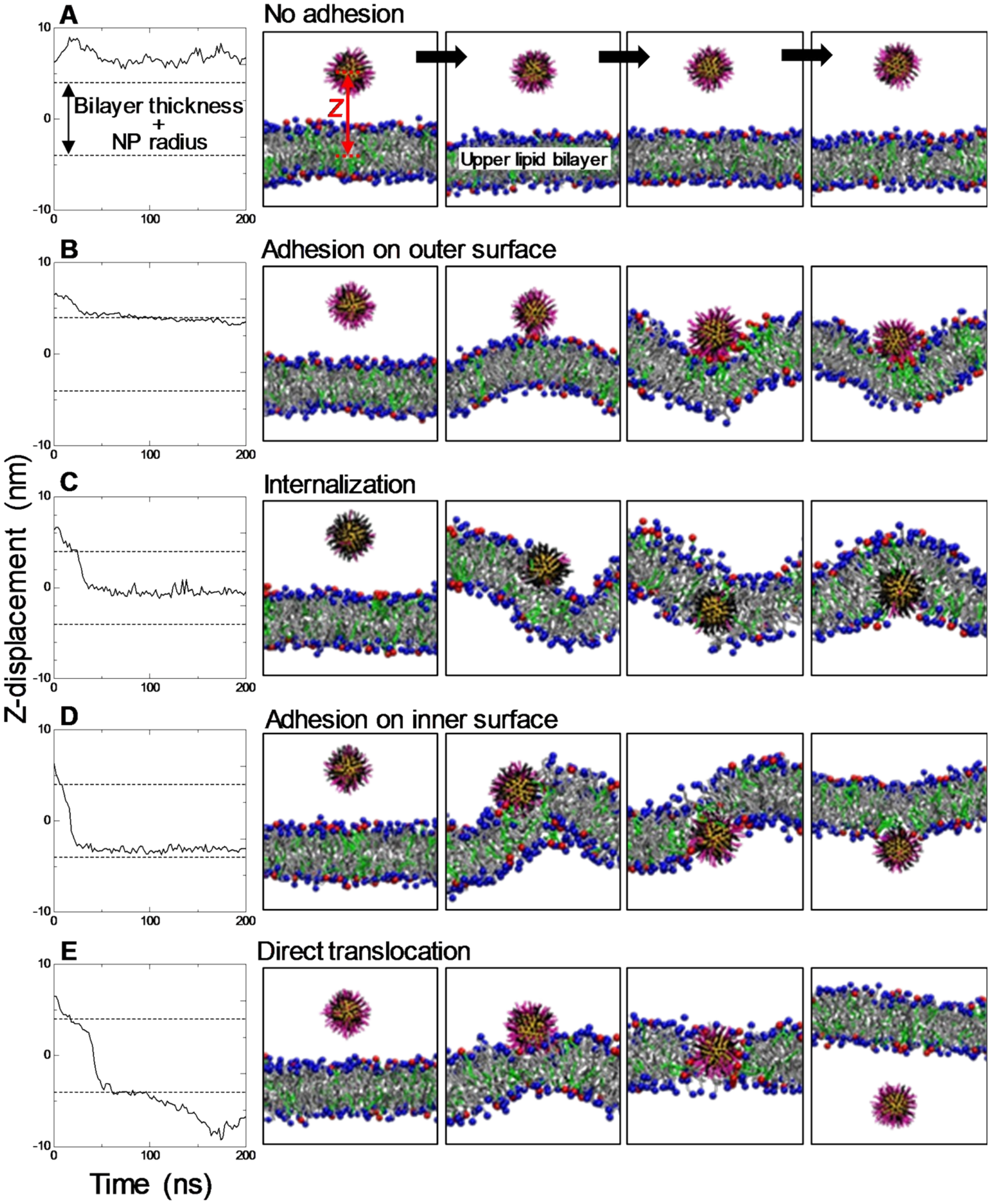

Fig. S4. Examples of five modes of the final locations of the NP: (A) no adhesion (diffusion in the outer solvent compartment); (B) adhesion on surface of the outer surface of the lipid bilayer; (C) internalization in the bilayer core; (D) adhesion on surface of the inner surface of the lipid bilayer; (E) direct translocation with self-resealing of the membrane. Water and ions are not shown for clarity. Each mode was classified according to the *Z*-displacement, which is the displacement from center of the upper lipid bilayer to the NP center.

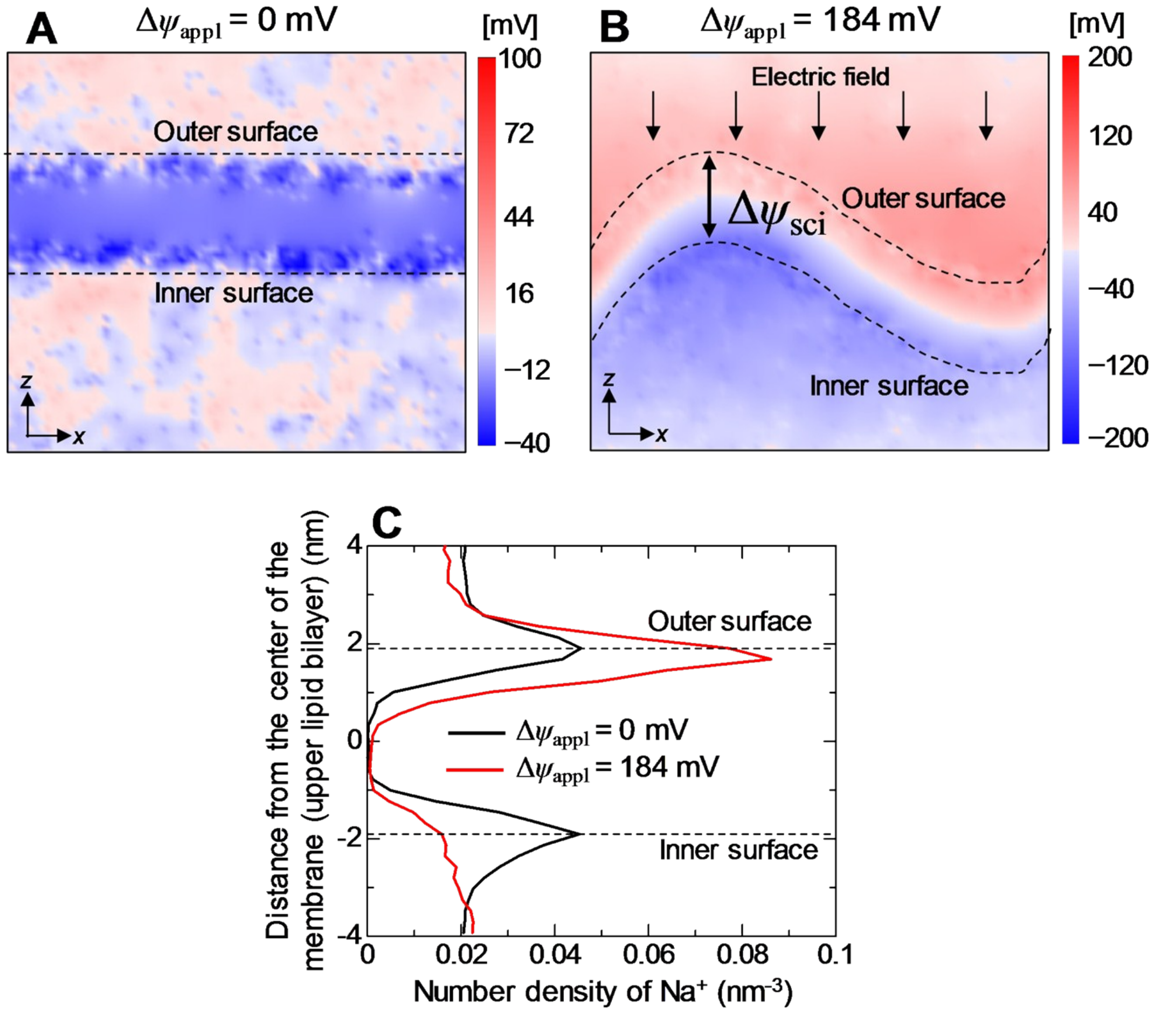

Fig. S5. Membrane potential arising from imbalance of the membrane surface charge ($\Delta\psi_{\mathrm{sci}}$). The distribution of electric potential $\psi(x)$ on a cross-section of the membrane (upper lipid bilayer) without NP at (A) $\Delta\psi_{\mathrm{appl}} = 0$ mV and (B) $\Delta\psi_{\mathrm{appl}} = 184$ mV. (C) Number density of cations (Na^+) along the membrane normal.

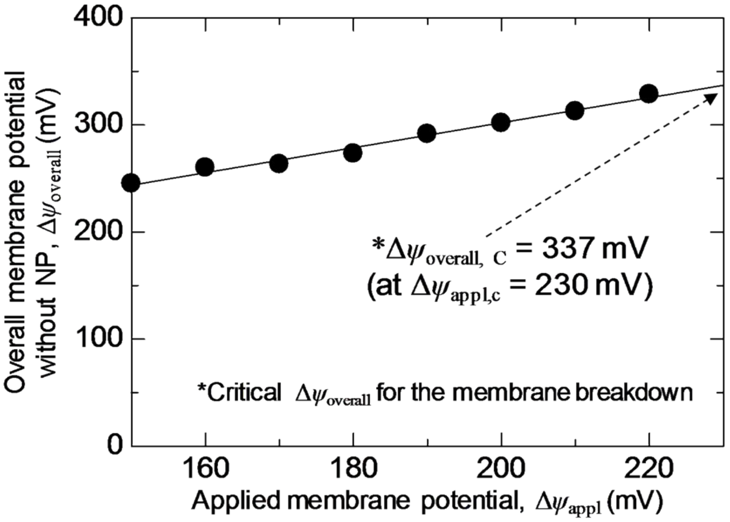

Fig. S6. Overall membrane potential ($\Delta\psi_{\text{overall}}$) without NP as a function of applied membrane potential ($\Delta\psi_{\text{appl}}$). The critical overall membrane potential for the membrane breakdown ($\Delta\psi_{\text{overall, C}}$) was determined by extrapolating the linear correlation between $\Delta\psi_{\text{overall}}$ and $\Delta\psi_{\text{appl}}$.

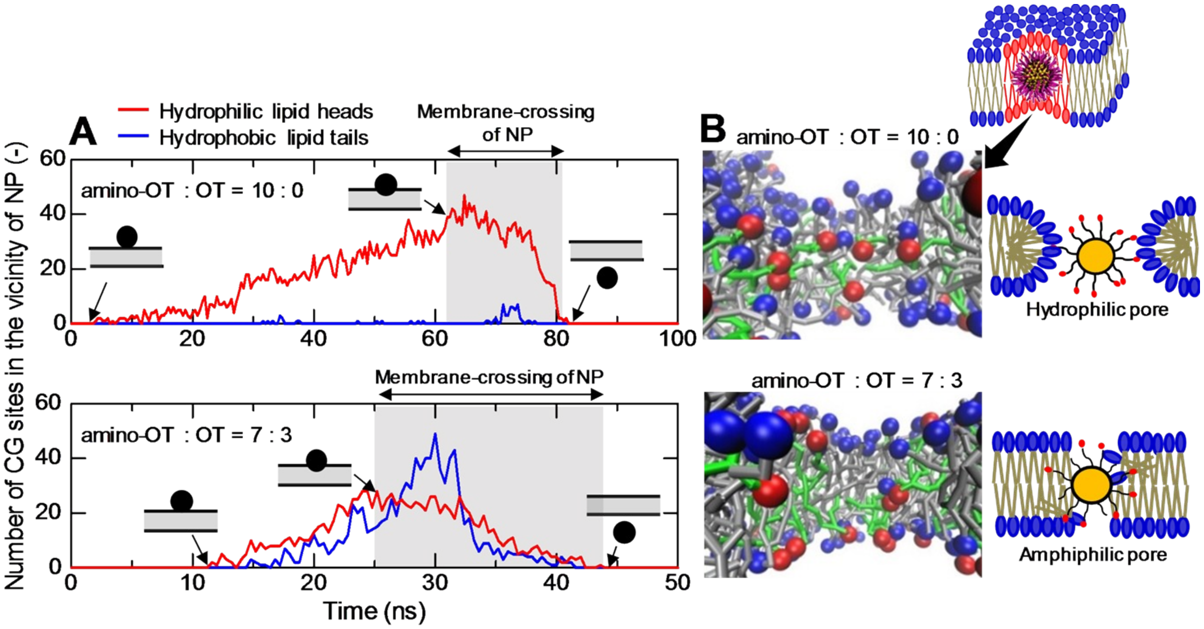

Fig. S7. Membrane-crossing of NPs with amino-OT:OT = 7:3 and 10:0. (A) Temporal change in the number of CG sites in the vicinity of NP with amino-OT:OT = 7:3 and 10:0 during the membrane-crossing of each NP. The lipid heads and tails existing within a radius of 2.00 nm from center of the NP were counted. (B) Morphology of the lipid molecules in the vicinity of each NP as the NP passed across the center of bilayer. The NP, water, and ions are not displayed for clarity. Beads and chains represent hydrophilic lipid heads and hydrophobic lipid tails, respectively. Blue beads and gray chains represent DPPC molecules. Red beads and green chains represent DPPG molecules.

Table S1. Comparison of membrane-translocation pathways of nanoparticles.

	Our previous study[1]	Electroporation	Endocytosis
Driving force	Weak external electric potential (0.1-0.2 V)	Extremely high electric potential (1000 – 1500 V)	Intrinsic cellular function
NP translocation dynamics	Translocating through pore formed during membrane-crossing of NP	Translocating through pore formed in advance of membrane-crossing of NP	Wrapped and enclosed by membrane vesicle
Cell membrane after translocation	Self-resealing of transmembrane pore (less damage)	Persistent transmembrane pore (higher damage)	Without poration (less damage)
Location of NP after translocation	Direct delivery to cytosol (higher delivery efficacy)	Directly delivery to cytosol (higher delivery efficacy)	Trapped by membrane vesicle (lower delivery efficacy)

Table S2. Molecular composition of the simulated system.

Number of total lipid molecules	2,304	(-)
Number of DPPC molecules	1,936	(-)
Number of DPPG molecules	368	(-)
Number of CG-water sites	123,466	(-)
Number of CG-sodium ion sites in outer compartment	894	(-)
Number of CG-sodium ion sites in inner compartment	894	(-)
Number of CG-chloride ion sites in outer compartment	710+x	(-)
Number of CG-chloride ion sites in inner compartment	710	(-)
Number of nanoparticles	1	(-)

x = number of amino-OT on nanoparticle surface

Table S3. NP properties and applied bias voltage used in the pBLM experiments with NPs.

Ref.	NP's properties			Applied bias voltage
	Material	Size	Surface potential	
4	Multi-wall carbon nanotube	20 nm X 10 μm	N.D.	100 mV
5	Polystyrene latex	16 to 20 nm	-27 to 32 mV	100 mV
6	Silica	60 to 110 nm	-20 to -30 mV	AC voltage
7	Polystyrene latex	60 nm	35 mV	70 mV
8	Gold NP	1.4 to 15 nm	N.D.	150 mV

C. Supplementary References

1 K. Shimizu, H. Nakamura and S. Watano, *Nanoscale*, 2016, **8**, 11897–11906.

2 A. Zachowski, *Biochem. J.*, 1993, **294**, 1–14.

3 J. N. Sachs, P. S. Crozier and T. B. Woolf, *J. Chem. Phys.*, 2004, **121**, 10847.

4 C. Corredor, W.-C. Hou, S. a. Klein, B. Y. Moghadam, M. Goryll, K. Doudrick, P. Westerhoff and J. D. Posner, *Carbon*, 2013, **60**, 67–75.

5 A. Negoda, K. J. Kim, E. D. Crandall and R. M. Worden, *Biochim. Biophys. Acta - Biomembr.*, 2013, **1828**, 2215–2222.

6 Y. Liu, Z. Zhang, Q. Zhang, G. L. Baker and R. M. Worden, *Biochim. Biophys. Acta - Biomembr.*, 2014, **1838**, 429–437.

7 B. Lu, T. Smith and J. J. Schmidt, *Nanoscale*, 2015, **7**, 7858–7866.

8 J. Broda, J. Setzler, A. Leifert, J. Steitz, R. Benz, U. Simon and W. Wenzel, *Nanomedicine Nanotechnology, Biol. Med.*, 2016, **12**, 1409–1419.